LETTER

doi:10.1038/nature22811

Microscopy of the interacting Harper–Hofstadter model in the two-body limit

M. Eric Tai[1], Alexander Lukin[1], Matthew Rispoli[1], Robert Schittko[1], Tim Menke[1], Dan Borgnia[1], Philipp M. Preiss[1]†, Fabian Grusdt[1], Adam M. Kaufman[1] & Markus Greiner[1]

The interplay between magnetic fields and interacting particles can lead to exotic phases of matter that exhibit topological order and high degrees of spatial entanglement[1]. Although these phases were discovered in a solid-state setting[2,3], recent innovations in systems of ultracold neutral atoms—uncharged atoms that do not naturally experience a Lorentz force—allow the synthesis of artificial magnetic, or gauge, fields[4–10]. This experimental platform holds promise for exploring exotic physics in fractional quantum Hall systems, owing to the microscopic control and precision that is achievable in cold-atom systems[11,12]. However, so far these experiments have mostly explored the regime of weak interactions, which precludes access to correlated many-body states[4,13–17]. Here, through microscopic atomic control and detection, we demonstrate the controlled incorporation of strong interactions into a two-body system with a chiral band structure. We observe and explain the way in which interparticle interactions induce chirality in the propagation dynamics of particles in a ladder-like, real-space lattice governed by the interacting Harper–Hofstadter model, which describes lattice-confined, coherently mobile particles in the presence of a magnetic field[18]. We use a bottom-up strategy to prepare interacting chiral quantum states, thus circumventing the challenges of a top-down approach that begins with a many-body system, the size of which can hinder the preparation of controlled states. Our experimental platform combines all of the necessary components for investigating highly entangled topological states, and our observations provide a benchmark for future experiments in the fractional quantum Hall regime.

The Harper–Hofstadter Hamiltonian is a model for describing lattice systems in the presence of a gauge field. When such a system is populated with interacting particles, chiral many-body states can emerge in the ground state. Here we study this model on a real-space, finite lattice for which single-site- and single-particle-resolved control and imaging are possible. The versatility of our platform enables us to build chiral systems and then to tune the particle number within a chiral state atom-by-atom and to control the real-space lattice size (Fig. 1a). Similar experiments using photonics[19] and atomic lattices[20] with synthetic dimensions[14,15,21] have been able to access the single-particle limit, but interaction effects have not been reported.

We can incrementally study our system by probing the single-particle band structure in the presence of a magnetic flux and then incorporating interactions through inclusion of an additional atom. In the single-particle limit, we observe the two chiral bands that emerge in the presence of a ladder or strip geometry[22]. By engineering a well-defined initial state, we can preferentially load an atom into one of the chiral bands, which results in shearing in the propagation of the particle (Fig. 1b). This shearing indicates a coupling of the dynamics along the leg (x) and rung (y) directions of the ladder that is reminiscent of a Lorentz force.

In the two-particle regime, interactions between the particles modify the eigenspectrum such that states of both a scattering and bound nature emerge. These interactions provide an avenue through which states of a certain chirality can be preferentially populated, giving rise to chiral trajectories that would otherwise be absent, even in the presence of a gauge field (Fig. 1b). By using quantum gas microscopy[23,24], we experimentally identify the mechanisms through which interactions produce these chiral dynamics. Importantly, although the measurements performed here are non-equilibrium, the agreement between theory and experiment, in the presence of interactions, paves the way for equilibrium measurements of chiral ground states[11,25,26].

Our experiments begin with a two-dimensional Bose–Einstein condensate of ^{87}Rb atoms located at the focus of a high-resolution imaging system. We use this imaging system to project a square optical lattice with spacing $a = 680$ nm and to resolve the parity of atomic site occupations through fluorescence imaging. A digital micromirror device enables the projection of nearly arbitrary optical potentials[27], which we use in state preparation and to confine evolution to a $2 \times N$ ladder region, where N quantifies the leg (x) dimension of the ladder. On this platform, we realize the Harper–Hofstadter Hamiltonian:

$$\mathcal{H} = \frac{U}{2}\sum_{i,j}\hat{n}_{i,j}(\hat{n}_{i,j}-1) - \sum_{i,j}\left(K\mathrm{e}^{-i\phi_{i,j}}\hat{a}^{\dagger}_{i+1,j}\hat{a}_{i,j} + J\hat{a}^{\dagger}_{i,j+1}\hat{a}_{i,j} + \mathrm{h.c.}\right) \quad (1)$$

where U is an on-site, pairwise, repulsive interaction energy, K and J are tunnelling amplitudes between nearest neighbour sites, $\hat{a}^{\dagger}_{i,j}$, $\hat{a}_{i,j}$ and $\hat{n}_{i,j}$ are the creation, annihilation and number operators for site (i, j), with $i \in \mathbb{Z}$ and $j \in \{0, 1\}$ for a ladder geometry, and h.c. is the Hermitian conjugate. The spatially varying complex tunnelling phases, $\phi_{i,j} = \Phi i + \pi j$, are realized through the combination of a magnetic field gradient and a running lattice (a moving standing wave that is formed by the interference of two intersecting, non-degenerate beams) to drive Raman transitions[16,17]. The non-trivial net phase (hereafter, flux) Φ for a loop around a unit cell yields an effective magnetic field analogous to the Aharonov–Bohm phase that is acquired by a charged particle in a real magnetic field. The flux Φ is controlled in our system by the angle between the running lattice and the static lattice on which the atoms reside. Because the Raman (running) lattice is projected through the objective (Fig. 2a), we are able to dynamically tune the effective magnetic field from the weak- to strong-field limits within a single experiment, without having to change the wavelength of the laser. For the experiments that follow, we operate in the regime in which $K/h \approx 10$ Hz, $J/h \approx 30$ Hz and $U/h \approx 130$ Hz, with h being Planck's constant (see Supplementary Information).

We probe the chiral band structure of this system by studying single-particle dynamics[22]. An atom is repeatedly prepared in a known initial state and the density distribution is obtained for several evolution times[28]. By means of a Landau–Zener sweep, this atom is delocalized to create the ground state of the central rung subsystem, $|\psi_{\mathrm{initial}}\rangle_{1\mathrm{p}} = (\hat{a}^{\dagger}_{0,1} + \hat{a}^{\dagger}_{0,0})|\mathrm{vac}\rangle/\sqrt{2} \equiv \hat{a}^{\dagger}_{0,\mathrm{S}}|\mathrm{vac}\rangle$ where subscripts 'i,S' ('i,A') indicate the creation of a symmetric (anti-symmetric) superposition on rung i and $|\mathrm{vac}\rangle$ is the vacuum state. A sweep in the opposite direction would

[1]Department of Physics, Harvard University, Cambridge, Massachusetts 02138, USA. †Present address: Physikalisches Institut, Universität Heidelberg, 69120 Heidelberg, Germany.

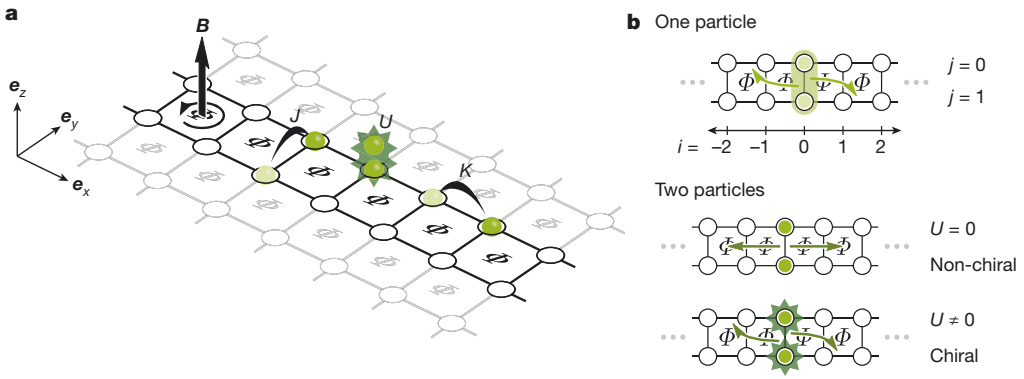

Figure 1 | Strongly interacting atoms in a gauge field. a, From a two-dimensional lattice (grey), we isolate a $2 \times N$ ladder region (black) in which we study the interacting Harper–Hofstadter model. Nearest-neighbour lattice sites in the x and y directions are coupled by complex- and real-valued tunnellings with magnitudes of K and J, respectively, realizing an artificial gauge field $\boldsymbol{B}$ with constant flux Φ per unit cell. The x, y and z directions are defined by the unit vectors $\boldsymbol{e}_x$, $\boldsymbol{e}_y$ and $\boldsymbol{e}_z$, respectively. When multiple atoms occupy the same lattice site, they experience a pairwise interaction shift U. **b**, We first study the motion of a single particle that is delocalized over two sites of a given rung (green shading). Owing to the coupling of motion in the x and y directions induced by the gauge field, chiral dynamics emerge through which rightward (leftward) motion is correlated with a bias towards the lower (upper) leg of the ladder, as illustrated by the green arrows. For comparison, a pair of non-interacting particles ($U = 0$) initialized onto opposite sides of a single rung is shown. In this case, the system does not exhibit chirality even in the presence of a gauge field. Finally, we study the addition of interactions between particles ($U \neq 0$) in the two-particle system. These interactions break the symmetry between particles moving to the left and to the right, thereby reintroducing chiral motion.

prepare $\hat{a}^\dagger_{0,\mathrm{A}}|\mathrm{vac}\rangle \equiv (\hat{a}^\dagger_{0,1} - \hat{a}^\dagger_{0,0})|\mathrm{vac}\rangle/\sqrt{2}$. From the initial state $\hat{a}^\dagger_{0,\mathrm{S}}|\mathrm{vac}\rangle$, we investigate the effect of the artificial magnetic field on the propagation dynamics of the atom after suddenly reducing the lattice depth in the x direction[14,15].

At zero flux, the motion of the particle is separable and so we expect no dynamics along the y direction because we prepared the atom in the ground state along this dimension. However, the coupling of a particle to a magnetic field gives rise to a non-separable Hamiltonian, yielding chirality and multi-dimensional dynamics in the motion of the atom. In Fig. 3b, the y components of the centre-of-mass (y_{COM}) for the left and right halves of the system are plotted as a function of evolution time. The density in both halves oscillates between the upper and lower legs of the ladder, but these oscillations occur out of phase with each other and are biased towards opposite legs. The population that propagates to the right (left) is initially biased towards the upper (lower) leg of the ladder—a behaviour that is reminiscent of skipping orbits.

We explain the chiral trajectories that are observed in the quantum walk using the band structure of the ladder. An isolated rung subsystem ($K = 0$) admits eigenstates with antisymmetric and symmetric superpositions of the atom occupying each constituent site, with the antisymmetric state being higher in energy by $2J$. In the limit that $J > K > 0$, these eigenstates hybridize with plane-wave states that run along the legs of the ladder such that there are two sub-bands with non-zero width of the order of K, split by an energy of the order of J (Fig. 3c). Each band is composed of Bloch states of quasi-momentum q, with the rung subsystems defining the unit cells of a one-dimensional lattice. The population of each site in the rung subsystems (colour scale in Fig. 3c) depends on the quasi-momentum of the eigenstate.

We identify the bands as $+$ or $-$ on the basis of their symmetric and antisymmetric character in the unperturbed $K = 0$ limit[22]. In the $+$ band, a population imbalance towards the upper (lower) leg of the ladder is associated with a rightward (leftward) group velocity, leading to chiral behaviour. The $-$ band exhibits the opposite chirality. The initial state shown in Fig. 3a more heavily populates the $+$ band, resulting in the chiral behaviour associated with that band. The converse would occur for the initial state $\hat{a}^\dagger_{0,\mathrm{A}}|\mathrm{vac}\rangle$.

We study the interplay between interparticle interactions and the synthetic gauge field by preparing two bosons on the two neighbouring sites of the central rung in the ladder. We express this initial state in terms of the single-particle states discussed above: $|\psi_{\mathrm{initial}}\rangle_{2\mathrm{p}} = \hat{a}^\dagger_{0,1}\hat{a}^\dagger_{0,0}|\mathrm{vac}\rangle = [(\hat{a}^\dagger_{0,\mathrm{S}})^2 - (\hat{a}^\dagger_{0,\mathrm{A}})^2]|\mathrm{vac}\rangle/\sqrt{2}$. This decomposition shows that the upper and lower chiral bands of Fig. 3c are equally populated. Hence, despite the presence of a gauge field, such a state would exhibit no chirality in the non-interacting limit because there is equal weight in bands of opposite chirality and because these weights are preserved in time as a result of the non-interacting eigenstates being products of the single-particle eigenstates. In contrast, we observe clear chiral orbits as the particles evolve from $|\psi_{\mathrm{initial}}\rangle_{2\mathrm{p}}$ in our experiment in which interactions play a critical part (Fig. 4a–c). By varying the flux with our projective scheme, we see that the observed chirality is present in the two-particle trajectories whenever the applied flux induces chirality in the single-particle bands (Fig. 4d), or specifically, when the flux Φ is neither zero nor π. Our data establishes that the observed chiral dynamics depend on both interparticle interactions and the applied gauge field.

To understand the way in which interactions introduce chirality into the dynamics of the two-particle quantum system, we delineate two classes of eigenstates. In one class, the bosons are bound through interactions. The other class corresponds to unbound scattering states in which the particles are largely independent and approximately equal to products of the single-particle eigenstates. We label this latter category $|++\rangle$, $|+-\rangle$ or $|--\rangle$, depending on the bands that are populated by the bosons. Because the bosons in our initial state are close to each other, we expect that there can be sizable overlaps with both types of eigenstates for our experimental parameters. To study the decomposition of the initial state experimentally, we measure the probability P_{11} for two bosons to occupy neighbouring sites of the same rung anywhere in the system as a function of time and gauge field strength (Fig. 5a). Even at long times we find a sizable, flux-dependent probability for the bosons to remain close to each other, consistent with the presence of a bound state.

To analyse which trajectories contribute most to the chiral signal, we study the shearing amplitude (as in Fig. 4c) as a function of the interparticle distance. At long times, we expect population in eigenstates of largely free-particle (bound) character to yield atoms that are farther apart (closer together). We find that shearing increases for bosons that are farther apart (Fig. 5b), which suggests that the populated, unbound scattering states contribute more to the observed chirality. This finding implies that there is an imbalance in the populations of $|++\rangle$ and $|--\rangle$ states. Given the stationary and equal population of the chiral bands in the non-interacting case, the imbalance in these observed dynamics must be induced by interactions. We confirm this conclusion by numerically calculating the overlap of our initial state with the eigenstates of the full interacting Hamiltonian, and the associated chirality

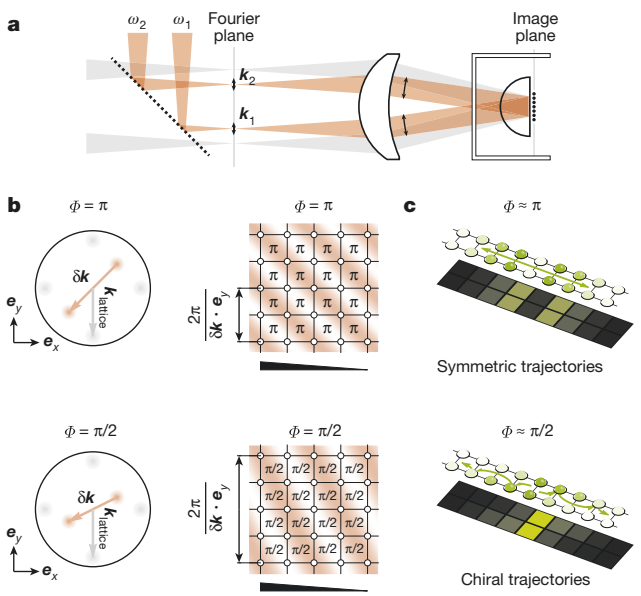

Figure 2 | Schematic of the experiments. Using a quantum gas microscope, we realize artificial gauge fields of variable strength by projecting a running (Raman) lattice with variable spacing through the same objective that was used to project the static (two-dimensional) lattice and image the atoms. **a**, A pair of beams (grey) interfere in the image plane of the microscope, creating one axis of the two-dimensional optical lattice. A pair of Raman beams (brown) with wavevectors $\boldsymbol{k}_1$ and $\boldsymbol{k}_2$ and slightly different frequencies ω_1 and ω_2 also interfere in the image plane, creating a Raman lattice. We adjust the periodicity and orientation of the Raman lattice by moving the position of the beams in the Fourier plane of the microscope. **b**, Examples of realizing fluxes of $\Phi = \pi$ (top) and $\Phi = \pi/2$ (bottom) in the system. In the Fourier plane of the microscope (left), grey and brown disks correspond to the beams used to create the two-dimensional and Raman lattices, respectively, with corresponding wavevectors $\boldsymbol{k}_{\mathrm{lattice}}$ and $\delta\boldsymbol{k} \equiv \boldsymbol{k}_1 - \boldsymbol{k}_2$. In this case, the ratio of the y component of the wavevector of the Raman lattice and the magnitude of the wavevector of the two-dimensional lattice determines the flux in the system[16,17]: $\delta\boldsymbol{k} \cdot \boldsymbol{e}_y/|\boldsymbol{k}_{\mathrm{lattice}}| = \Phi/\pi$. In the resulting image plane structure (right), the two-dimensional lattice is represented by the black grid and the brown shading represents the spatial intensity distribution of the Raman lattice at one instance in time. In this case, the product of the y component of the wavevector of the Raman lattice and the lattice constant a determines the flux in the system: $\delta\boldsymbol{k} \cdot a\boldsymbol{e}_y = \Phi$. The black triangle indicates the potential gradient imposed by a physical magnetic field, which is used to detune lattice sites along the x direction. **c**, Resultant dynamics for the example cases of fluxes of $\Phi \approx \pi$ (top) and $\Phi \approx \pi/2$ (bottom). The upper diagram in each example illustrates the time dynamics of the centre-of-mass for particles travelling to the left and to the right from the initial rung, with the shading corresponding to atomic density. The lower diagram is the measured density distribution following time evolution, with black corresponding to lower densities and green to higher densities. The density distribution for $\Phi \approx \pi/2$ demonstrates asymmetric propagation, whereas that for $\Phi \approx \pi$ demonstrates symmetric propagation.

$\mathcal{C}_n$ (see Supplementary Information) of these eigenstates (Fig. 5c, d). In addition, a short-time perturbative expansion shows that, to leading order in the evolution time t (see Supplementary Information), $y_{\mathrm{COM}}(t) = \pm a(2\pi t/h)^5(KJ)^2U\sin(\Phi)$ for the right (+) and left (−) side of the ladder, indicating that the dynamics depend on both the flux Φ and the interactions U.

To illustrate the process by which interactions induce a population imbalance between $|++\rangle$ and $|--\rangle$ scattering states, we analyse the eigenstates of two interacting bosons on the central rung and study the way in which they hybridize with delocalized states as the tunnel coupling K is introduced. In the limit $U \gg J$, two of the three two-boson eigenstates involve double occupancy of one site, causing an energy

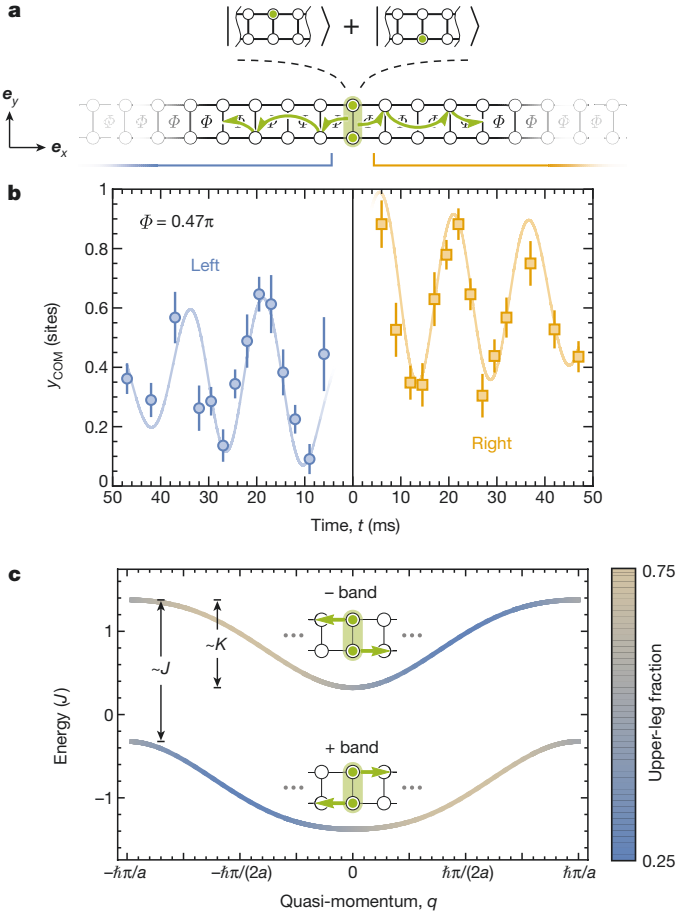

Figure 3 | Single-particle chiral dynamics and band structure. **a**, In the presence of a gauge field, a particle that is initially delocalized across a single rung (top) exhibits chiral motion (an exemplary trajectory is indicated by the green arrows). **b**, To quantify the chiral dynamics, we track the time evolution of the x and y components of the centre-of-mass (x_{COM} and y_{COM}) for the left (blue) and right (orange) halves of the system for a flux of $\Phi = 0.47\pi$. Population on the initial rung is always excluded from the centre-of-mass determination. Although the particle symmetrically delocalizes over multiple sites in the x direction (see Supplementary Information), its motion in the y direction is asymmetric with respect to the central rung. The data (filled circles and squares) are well matched by exact diagonalization of the Harper–Hofstadter model (solid lines), which was performed for our system with the tunnellings fitted to $K/h = 12(1)$ Hz and $J/h = 29(2)$ Hz (see Supplementary Information). Owing to technical errors in the preparation of the initial state (see Supplementary Information), the chiral trajectory is slightly modified from the case of a symmetric superposition. The error bars correspond to the standard error. **c**, Band structure computed for the simulation parameters used in **b**. The spectrum exhibits two bands with width of the order of K, split by an energy of the order of J, with the upper-leg population fraction of each eigenstate encoded by the colour scale. In each band, there is a correlation between the sign of the group velocity and the leg towards which the particle is biased. However, the sign of the correlation differs between the two bands, giving rise to chiral bands of opposite sign, which we denote by + and −. The states that make up the + (−) band are plane-wave states with a mostly symmetric (antisymmetric) delocalization across the constituent rungs and a quasi-momentum-dependent admixture ϵ_q of the symmetric (antisymmetric) delocalization: $(|S\rangle + \epsilon_q|A\rangle) \otimes |q\rangle$ $((|A\rangle + \epsilon_q|S\rangle) \otimes |q\rangle)$. The chirality of each band is shown in the insets, with particles preferentially sticking to one of the legs depending on the propagation direction. For the example shown in **b**, the initial state preferentially populates the lower band, resulting in chiral dynamics associated with that band.

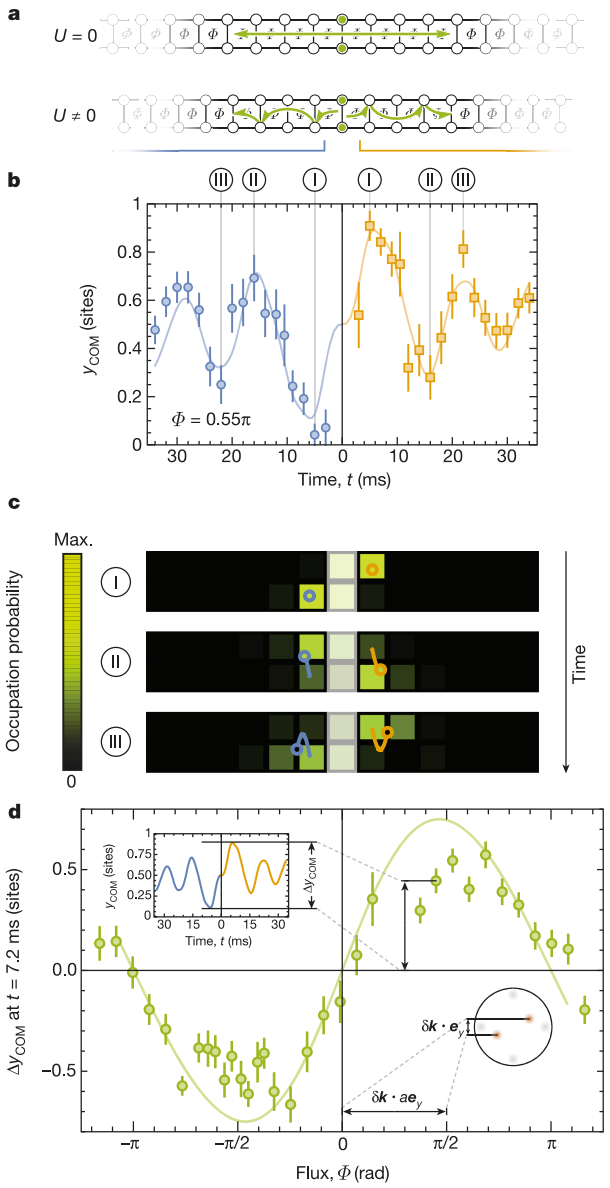

Figure 4 | Interacting chiral trajectories. a, We initialize two particles on opposite sides of the central rung and track the density distribution in the presence of a gauge field. The interactions ($U \neq 0$) lead to chirality in the propagation dynamics. **b**, The interaction-induced chirality manifests in the y component of the centre-of-mass y_{COM}; data for the left and right halves of the system are shown in blue and orange, respectively. The solid lines result from an exact diagonalization at $\Phi = 0.55\pi$ with $U/h = 131.2(6)$ Hz, $J/h = 34.1(6)$ Hz and $K/h = 11(1)$ Hz, each of which are obtained from independent calibrations. **c**, Exemplary density distributions at the times indicated in **a**. The colour of a given square indicates the occupation probability of that lattice site normalized to the total population in its half of the system (L, left; R, right), $\langle \hat{n}_{i,j} \rangle / \left(\sum_{i,j \in \mathrm{L,R}} \langle \hat{n}_{i,j} \rangle \right)$; 'Max.' refers to the maximum average density on either the left or right side. Blue (orange) circles indicate the position of the centre-of-mass at the given point in time for the left (right) half; solid lines trace its evolution over earlier times. **d**, We quantify the amount of chirality by the shearing Δy_{COM} at $t = 7.2$ ms, which roughly corresponds to the first maximum in the evolution of the centre-of-mass y_{COM} for all Φ (see upper inset). Our data (green circles) shows that chirality is absent for fluxes of $\Phi \approx 0$ and $\Phi \approx \pi$, highlighting the role of the gauge field in the chiral dynamics. To further illustrate our projection scheme, in the lower inset we show where the Raman lattice beams (brown disks) are situated in the Fourier plane to realize a flux of $\Phi = \delta \boldsymbol{k} \cdot a \boldsymbol{e}_y \approx \pi/2$ in the image plane. The solid line results from an exact diagonalization with the parameters used in **b**, carried out at the independently calibrated flux values. The error bars in **b** and **d** correspond to the standard error.

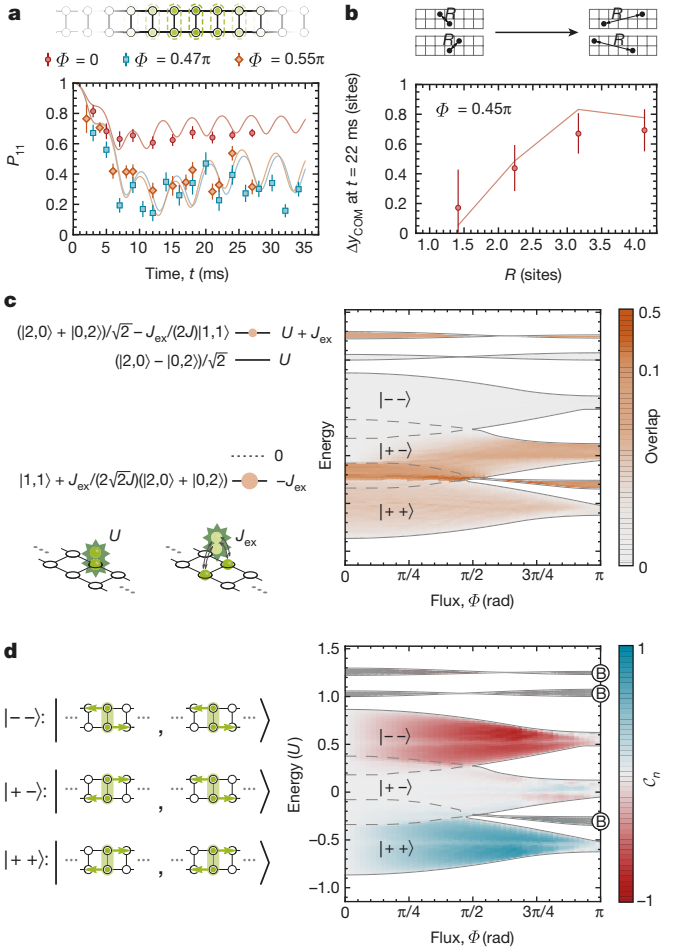

Figure 5 | Physical mechanism for chirality with interactions. The interacting two-particle dynamics give rise to bound and scattering states. The solid lines (**a**, **b**) and coloured regions (**c**, **d**) are obtained from exact diagonalization, with the independently calibrated values $U/h = 131.2(6)$ Hz, $J/h = 34.1(6)$ Hz and $K/h = 11(1)$ Hz at the indicated flux values. **a**, We plot the probability P_{11} that the particles are on different sites of the same rung (see schematic above the plot) as a function of time and flux; this quantity provides a measure of the population in the lowest-energy bound state (see **d**). The dynamics in P_{11} are shown for fluxes of $\Phi = 0$, $\Phi = 0.47\pi$ and $\Phi = 0.55\pi$. **b**, The degree of shearing Δy_{COM} after 22 ms of evolution in the ladder is plotted as a function of the interparticle spacing R (see schematic above the plot), that is, the average Δy_{COM} when the atoms are a distance R apart. The shearing, a proxy for the chirality, suggests that the scattering states in which particles are further separated contribute most to the chirality. The error bars in **a** and **b** correspond to the standard error in the associated measurement. **c**, We show the population of the eigenstates of the initial rung in the $K = 0$ limit, where $|i, j\rangle = \hat{a}^{\dagger}_{0,i} \hat{a}^{\dagger}_{0,j} |\mathrm{vac}\rangle$, and also how these eigenstates are energetically situated in terms of U and the super-exchange energy J_{ex} (left). We also show the full many-body spectrum as a function of flux, given the calibrated J, K and U (right). The left and right panels are energetically aligned to scale. The colour scale encodes the overlap between our initial state and these many-body eigenstates, with the boundaries of the different eigenstate regions of interest delineated by grey lines. The regions enclosing $|- -\rangle$, $|+ -\rangle$ and $|+ +\rangle$ are largely described by product states of the unbound eigenstates. **d**, Chiral character of the many-body eigenstates. The + and − labels indicate the single-particle band that mostly describes the coloured bands in the plot; the composite two-particle states are illustrated on the left. The colour scale denotes the chirality $\mathcal{C}_n$ of the eigenstates within the bands (see Supplementary Information). The dark grey regions (labelled 'B') refer to the eigenstates that make up the bound states in the ladder system; the other states are scattering states.

shift of order U (Fig. 5c). These states are detuned from the delocalized states and do not influence the dynamics. There is a third eigenstate near zero energy with large overlap with our initial state. Owing to the finite J and U, this eigenstate is shifted down in energy by $J_{ex} = 4J^2/U$ through a super-exchange process (Fig. 5c). For $U = 0$, the tunnel coupling K along the legs hybridizes this rung eigenstate equally with $|--\rangle$ and $|++\rangle$ states. Because of the downward energy shift of J_{ex} for $U \neq 0$, the third eigenstate is energetically closer to the $|++\rangle$ states and hybridizes primarily with this chiral band (Fig. 5c). The interactions also create a delocalized bound state when $J_{ex} \approx K$, corresponding to a particle on each site of a rung somewhere in the system, which is reflected by the non-vanishing P_{11}. As the flux Φ is increased, the motion of particles in the x and y directions becomes increasingly coupled by the gauge field, leading to additional hybridization with the $|+-\rangle$ states (Fig. 5c). This effect is also in agreement with the observed reduction of P_{11} at long times when introducing the gauge field (Fig. 5a).

In conclusion, the combination of interparticle interactions and a synthetic gauge field leads to our observation of chirality in the two-particle dynamics. Our observations depend on the interactions being finite—neither vanishing nor infinite. In either case, there is no exchange-energy shift J_{ex}, leading to equal populations in the two chiral sectors. Operating in a regime in which the interactions and gauge field work in concert is crucial to accessing chiral Mott insulators and fractional quantum Hall physics. Regarding the latter, our use of a real-space lattice enables us to achieve isotropic interactions in a scalable, versatile geometry, closely corresponding to the condensed matter systems in which this exotic physics was discovered. Finally, the dynamically tunable flux and site-resolved detection and manipulation realized in our experiments are valuable tools for generating and characterizing topological phases of matter[29].

Online Content Methods, along with any additional Extended Data display items and Source Data, are available in the online version of the paper; references unique to these sections appear only in the online paper.

Data Availability The data that support the findings of this study are available from the corresponding author upon reasonable request.

Received 6 December 2016; accepted 1 May 2017.

1. Chen, X., Gu, Z.-C. & Wen, X.-G. Local unitary transformation, long-range quantum entanglement, wave function renormalization, and topological order. *Phys. Rev. B* **82,** 155138 (2010).
2. Tsui, D. C., Stormer, H. L. & Gossard, A. C. Two-dimensional magnetotransport in the extreme quantum limit. *Phys. Rev. Lett.* **48,** 1559–1562 (1982).
3. Laughlin, R. B. Anomalous quantum Hall effect: an incompressible quantum fluid with fractionally charged excitations. *Phys. Rev. Lett.* **50,** 1395–1398 (1983).
4. Schweikhard, V., Coddington, I., Engels, P., Mogendorff, V. P. & Cornell, E. A. Rapidly rotating Bose-Einstein condensates in and near the lowest Landau level. *Phys. Rev. Lett.* **92,** 040404 (2004).
5. Lignier, H. *et al.* Dynamical control of matter-wave tunneling in periodic potentials. *Phys. Rev. Lett.* **99,** 220403 (2007).
6. Jaksch, D. & Zoller, P. Creation of effective magnetic fields in optical lattices: the Hofstadter butterfly for cold neutral atoms. *New J. Phys.* **5,** 56 (2003).
7. Kolovsky, A. R. Creating artificial magnetic fields for cold atoms by photon-assisted tunneling. *Europhys. Lett.* **93,** 20003 (2011).
8. Lin, Y.-J., Compton, R. L., Jiménez-Garca, K., Porto, J. V. & Spielman, I. B. Synthetic magnetic fields for ultracold neutral atoms. *Nature* **462,** 628–632 (2009).
9. An, F. A., Meier, E. J. & Gadway, B. Direct observation of chiral currents and magnetic reflection in atomic flux lattices. *Sci. Adv.* **3,** e1602685 (2017).
10. Kolkowitz, S. *et al.* Spin–orbit-coupled fermions in an optical lattice clock. *Nature* **542,** 66–70 (2017).
11. Hafezi, M., Sørensen, A. S., Demler, E. & Lukin, M. D. Fractional quantum Hall effect in optical lattices. *Phys. Rev. A* **76,** 023613 (2007).
12. Gemelke, N., Sarajlic, E. & Chu, S. Rotating few-body atomic systems in the fractional quantum Hall regime. Preprint at https://arxiv.org/abs/1007.2677 (2010).
13. Jotzu, G. *et al.* Experimental realization of the topological Haldane model with ultracold fermions. *Nature* **515,** 237–240 (2014).
14. Stuhl, B. K., Lu, H.-I., Aycock, L. M., Genkina, D. & Spielman, I. B. Visualizing edge states with an atomic Bose gas in the quantum Hall regime. *Science* **349,** 1514–1518 (2015).
15. Mancini, M. *et al.* Observation of chiral edge states with neutral fermions in synthetic Hall ribbons. *Science* **349,** 1510–1513 (2015).
16. Aidelsburger, M. *et al.* Realization of the Hofstadter Hamiltonian with ultracold atoms in optical lattices. *Phys. Rev. Lett.* **111,** 185301 (2013).
17. Miyake, H., Siviloglou, G. A., Kennedy, C. J., Burton, W. C. & Ketterle, W. Realizing the Harper Hamiltonian with laser-assisted tunneling in optical lattices. *Phys. Rev. Lett.* **111,** 185302 (2013).
18. Harper, P. G. Single band motion of conduction electrons in a uniform magnetic field. *Proc. Phys. Soc. A* **68,** 874–878 (1955).
19. Hafezi, M., Mittal, S., Fan, J., Migdall, A. & Taylor, J. M. Imaging topological edge states in silicon photonics. *Nat. Photon.* **7,** 1001–1005 (2013).
20. Leder, M. *et al.* Real-space imaging of a topologically protected edge state with ultracold atoms in an amplitude-chirped optical lattice. *Nat. Commun.* **7,** 13112 (2016).
21. Celi, A. *et al.* Synthetic gauge fields in synthetic dimensions. *Phys. Rev. Lett.* **112,** 043001 (2014).
22. Hügel, D. & Paredes, B. Chiral ladders and the edges of quantum Hall insulators. *Phys. Rev. A* **89,** 023619 (2014).
23. Bakr, W. S., Gillen, J. I., Peng, A., Fölling, S. & Greiner, M. A quantum gas microscope for detecting single atoms in a Hubbard-regime optical lattice. *Nature* **462,** 74–77 (2009).
24. Sherson, J. F. *et al.* Single-atom-resolved fluorescence imaging of an atomic Mott insulator. *Nature* **467,** 68–72 (2010).
25. Dhar, A. *et al.* Bose-Hubbard model in a strong effective magnetic field: emergence of a chiral Mott insulator ground state. *Phys. Rev. A* **85,** 041602 (2012).
26. Roushan, P. *et al.* Chiral ground-state currents of interacting photons in a synthetic magnetic field. *Nat. Phys.* **13,** 146–151 (2017).
27. Zupancic, P. *et al.* Ultra-precise holographic beam shaping for microscopic quantum control. *Opt. Express* **24,** 13881–13893 (2016).
28. Preiss, P. M. *et al.* Strongly correlated quantum walks in optical lattices. *Science* **347,** 1229–1233 (2015).
29. He, Y.-C., Grusdt, F., Kaufman, A., Greiner, M. & Vishwanath, A. Realizing and Adiabatically Preparing Bosonic Integer and Fractional Quantum Hall states in Optical Lattices. Preprint at https://arxiv.org/abs/1703.00430 (2017).

Supplementary Information is available in the online version of the paper.

Acknowledgements We acknowledge conversations with M. Aidelsburger, I. Cirac, E. Demler, M. Endres, M. Foss-Feig, N. Gemelke, D. Greif, W. Ketterle, R. Ma, H. C. Po, J. Simon and A. Vishwanath. We are supported by grants from the National Science Foundation, the Gordon and Betty Moore Foundation's EPiQS Initiative, an Air Force Office of Scientific Research MURI programme, an Army Research Office MURI programme and the NSF Graduate Research Fellowship Program (M.R.).

Author Contributions M.E.T., A.L., M.R., R.S., P.M.P. and A.M.K. contributed to constructing the experiment, collecting and analysing the data, and writing the manuscript. F.G. and T.M. contributed to analysing the data and writing the manuscript. D.B. developed the short-time analytic result. M.G. supervised the work.

Author Information Reprints and permissions information is available at www.nature.com/reprints. The authors declare no competing financial interests. Readers are welcome to comment on the online version of the paper. Publisher's note: Springer Nature remains neutral with regard to jurisdictional claims in published maps and institutional affiliations. Correspondence and requests for materials should be addressed to M.G. (greiner@physics.harvard.edu).

Reviewer Information *Nature* thanks L. LeBlanc and the other anonymous reviewer(s) for their contribution to the peer review of this work.